WILEY-VCH

Integrated water and thermal managements in bioinspired hierarchical MXene aerogels for highly efficient solar-powered water evaporation

Hongming Zhang, Xi Shen, Eunyoung Kim, Mingyue Wang, Jeng-Hun Lee, Haomin Chen, Guangcheng Zhang, Jang-Kyo Kim**

Dr. H.M. Zhang, E.Y. Kim, Dr. M.Y. Wang, Dr. J.-H. Lee, H.M. Chen, Prof. J.-K. Kim
Department of Mechanical and Aerospace Engineering, The Hong Kong University of Science and Technology, Clear Water Bay, Kowloon, Hong Kong
E-mail: mejkkim@ust.hk (J.-K. Kim)

Dr. X. Shen
Department of Aeronautical and Aviation Engineering, The Hong Kong Polytechnic University, Hung Hom, Kowloon, Hong Kong
E-mail: xi.shen@polyu.edu.hk

Dr. H.M. Zhang, Prof. G. Zhang
Shaanxi Key Laboratory of Macromolecular Science and Technology, School of Chemistry and Chemical Engineering, Northwestern Polytechnical University, Xi'an, Shaanxi, 710072, PR China

H.M. Zhang and X. Shen contribute equally to this work.

Keywords: MXene, aerogel, hierarchical structure, thermal insulation, solar-powered water evaporation

Abstract

Solar-powered water evaporation is a straightforward, practical approach to use solar energy for water desalination. Solar absorbers made from photothermal materials capable of effectively confining heat and pumping water to the evaporation surface are essential for a high energy efficiency. However, separate designs of water transport routes and thermal insulating layers are required to simultaneously achieve desired water and thermal managements. This work reports an integrated design for efficient multifunctional capabilities through rational assembly of spectrally modified $Ti_3C_2T_x$ (SM-$Ti_3C_2T_x$) nanosheets and polyvinyl alcohol (PVA) into a multiscale 3D aerogel with a feather-like microstructure. The aerogel contains longitudinal struts with transversely parallel ligaments developed at an angle of ~ 60° from the struts, resembling the microstructure of down feathers in penguins and thus leading to excellent thermal insulation. The hydrophilic porous ligaments serve as upward water transport channels,

This is the peer reviewed version of the following article: Zhang, H. M., Shen, X., Kim, E. Y., Wang, M. Y., Lee, J.-H., Chen, H. M., Zhang, G., Kim, J.-K., Integrated Water and Thermal Managements in Bioinspired Hierarchical MXene Aerogels for Highly Efficient Solar-Powered Water Evaporation. Adv. Funct. Mater. 2022, 32, 2111794, which has been published in final form at https://doi.org/10.1002/adfm.202111794.

pumping the water to the evaporation surface while confining it within the ligaments to avoid oversaturation. These functional features endow the composite aerogel with a high energy efficiency of 88.52 % and an evaporation rate of 0.92 kg m^{-2} h^{-1} at a weak solar irradiance of 0.5-sun, promising its great potential for practical solar-powered water desalination under natural sunlight.

1. Introduction

Solar energy is an abundant, renewable energy source boasting to be a sustainable and environmentally friendly alternative to conventional energy sources such as fossil fuels. The solar-powered water evaporation strategy directly utilizes the thermal energy generated from the sun to harvest solar energy for water desalination and purification.[1] Compared to existing desalination and water treatment techniques, this strategy consumes no extra energy other than solar energy and does not require large infrastructures to implement. Therefore, it is considered a promising technology for producing clean water in less-developed regions. In the application of this technology, efficient utilization of solar energy is usually achieved using a solar absorber floating on water to generate and confine the heat at water-air interfaces for interfacial water evaporation.[2] To attain a high solar-to-vapor energy conversion efficiency and evaporation rate, the solar absorbers need to fulfill three requirements concurrently, namely, (i) a high optical absorption in the solar wavelengths of 0.3 to 2.5 μm to maximize the solar-to-thermal conversion; (ii) an excellent thermal management to minimize the heat loss; and (iii) a proper water management to ensure sufficient water supply to the evaporation surface. To render a high solar-to-thermal conversion, photothermal materials with broadband sunlight absorption including plasmonic nanoparticles,[3,4] semiconductors,[5,6] and carbon nanomaterials[7–15] have been widely used. Most recently, MXene, a family of 2D titanium carbides or nitrides, have been considered as promising photothermal materials because of its excellent light-to-thermal

conversion efficiency of nearly 100 %.[16–23] Various absorbers in the form of membranes,[20,23] aerogels,[18,19,21] and hydrogels[17,22,24] have been made from 2D MXene sheets for achieving a high photothermal efficiency. Nevertheless, their application is still limited by the mediocre optical absorption in the solar wavelengths. Other photothermal materials, such as carbon nanomaterials and plasmonic nanoparticles, had to be used in combination with MXene to achieve broadband absorption,[17,18,20,22] inevitably complicating the fabrication process. To further the application of MXene, novel strategies need to be developed to improve its sunlight absorption without additional fillers.

Myriad efforts have been made to rationally construct three-dimensional (3D) porous solar absorbers using the abovementioned photothermal materials for simultaneously high sunlight absorption, efficient water supply, and proper thermal management.[2,25,26] Several strategies have been implemented for the effective thermal management by 3D absorbers including heat extraction from bulk water,[27] harvesting energy from air,[28,29] and latent heat recycling,[30] significantly reducing the heat loss to the environment during evaporation. By optimizing the compositions and microstructures of 3D absorbers,[31–35] fast water transport and moderate heat loss have been achieved, leading to high solar-to-vapor energy efficiencies of over 90% under a standard incident light intensity of 1-sun (*i.e.*, 1 kW m^{-2}).[4,10,18,36] However, absorbers in practical applications are exposed under the natural sunlight, which typically has a light intensity lower than 1-sun depending on various factors including seasons, weather conditions and locations.[11,37] Unfortunately, 3D absorbers performing well under 1-sun exhibited a significantly impaired energy efficiency at lower light intensities, primarily due to the heat losses arising from the unsatisfactory thermal management.[19] Given that the actual thermal energy available for evaporation is equivalent to the incident solar energy subtracted by the heat loss, a moderate amount of heat loss – which may be trivial under the standard 1-sun – can substantially reduce the actual thermal energy for evaporation when the incident light

intensity is lower. Therefore, it is of paramount importance to further reduce the heat loss while maintaining fast water transport in the 3D absorbers to achieve a high energy efficiency even at a low sunlight intensity for practical water production.

Nevertheless, the conflicting requirements for fast water transport and low heat loss make it very challenging to achieve both attributes in the same 3D absorber. For fast water transport, 3D structures were commonly designed with vertically-aligned pores to directly pump the water to the evaporation surface.[38] However, such a direct water pathway inevitably sacrifices the heat localization because the vertically-aligned pore walls facilitate fast downward heat conduction from the evaporation surface to bulk water.[13,17,21,22,39] In addition, hydrophilic cell walls designed for fast water uptake also led to oversaturated water, aggravating the convective heat loss.[40,41] These conductive and convective heat losses in turn gave rise to mediocre solar-to-vapor efficiencies of less than 85% at a weak solar irradiance of 0.5-sun for most of the available 3D absorbers.[19,36,42–46] On one hand, although confining water molecules in nanochannels effectively reduced the vaporization enthalpy and improved the energy efficiency to 88.4 % under 0.5-sun,[37] additional insulating foams were used to help suppress the heat loss, making the whole system bulky for large-scale deployment. On the other hand, longitudinally-layered channels were more effective in blocking the heat conduction than the vertical channels,[47] but could not effectively pump water to the evaporation surface due to the horizontal water transport pathways, resulting in an energy efficiency of lower than 80% even at 1-sun. In other words, all the existing structural designs for water and thermal managements have been implemented independently, hence simultaneously achieving fast water transport and mitigated heat loss for high energy efficiencies at low sunlight intensities highly challenging using the same 3D absorber.

Here, we propose an integrated design strategy for concurrent water and thermal managements by tailoring both wall structures and porous channels in a 3D aerogel absorber. $Ti_3C_2T_x$

nanosheets, a typical type of MXene, were chemically modified by leveraging their natural oxidation process to readily augment the absorption spectra in the whole solar wavelengths. The spectrally modified $Ti_3C_2T_x$ (SM-$Ti_3C_2T_x$) nanosheets were assembled into a 3D aerogel by a novel 'ice-structuring freeze-casting' (ISFC) technique using polyvinyl alcohol (PVA) as additive to control the ice structure during growth. The aerogel had an anisotropic hierarchical structure consisting of longitudinal struts connected by transverse ligaments resembling that of down feathers in penguins, leading to excellent thermal insulation transverse to the struts. The parallel, transverse ligaments comprising highly hydrophilic SM-$Ti_3C_2T_x$ nanosheets and PVA served as vertical water transport channels, pumping the water to the evaporation surface while avoiding the oversaturation of water by confining it within the ligaments. The simultaneous broadband sunlight absorption, thermal management and water regulation achieved in the SM-$Ti_3C_2T_x$/PVA aerogel contributed to a high energy efficiency of 88.52 % with an evaporation rate of 0.92 kg m^{-2} h^{-1} at a weak solar irradiance of 0.5-sun, demonstrating great potential for practical solar-powered water desalination and purification under natural sunlight.

2. Results and discussion

2.1. Biomimetic design of down feather-like SM-$Ti_3C_2T_x$/PVA aerogels

Penguins possess a unique feather structure to keep their bodies warm in an extreme cold environment.[48] As shown in **Figure 1**a, the down feather responsible for thermal insulation features a unique hierarchical structure consisting of aligned long rami and parallel short barbules developing at an angle of 60 to 80° from the ramus.[49] The interaction between barbules creates abundant air pockets, effectively extenuating conductive, convective and radiative heat losses from the penguin body.[50,51] Inspired by penguin's natural protection strategy, we designed an anisotropic aerogel with a microstructure resembling that of penguin's down feather to circumvent heat losses (**Figure 1**b), which is critical for a high solar-to-vapor energy efficiency under weak sunlight. To achieve the desired microstructure, a novel ISFC

technique was developed to assemble SM-$Ti_3C_2T_x$ and PVA into an aerogel (**Figure 1**c). The mixture of PVA and SM-$Ti_3C_2T_x$ was freeze-thawed three times to obtain a hydrogel, which was subsequently freeze-cast unidirectionally and freeze-dried to form an SM-$Ti_3C_2T_x$/PVA aerogel. Unlike the conventional unidirectional freeze-casting technique which produces lamellar cell walls,[52] the ISFC technique used PVA as an ice-structuring binder to induce dendritic growths of ice crystals from the main trunks.[53] The higher viscosity of freezing solution because of the addition of PVA and the repeated freezing-thawing process discouraged the growth of main trunks along the temperature gradient while facilitating the formation of transverse ligaments at an angle to the main trunks.[54] Therefore, the resulting SM-$Ti_3C_2T_x$/PVA composite aerogel exhibited a unique feather-like structure consisting of longitudinal struts in the freezing direction and transversely parallel ligaments at an angle of ~ 60° from the struts (**Figure 1**b). The microstructure endowed the aerogel with concurrent, multifunctional capabilities including the thermal management and water regulation, as shown in **Figure 1**d. The unique features include: (i) the longitudinal main struts aligned horizontally with slanted short ligaments to create porous channels for effective thermal insulation; (ii) the hydrophilic ligaments made of SM-$Ti_3C_2T_x$ and PVA interconnected in the thickness direction for effective water uptake while avoiding the oversaturation of water by confining the water within the ligaments; and (iii) the optimal ligament compositions and structures for maximized sunlight absorption.

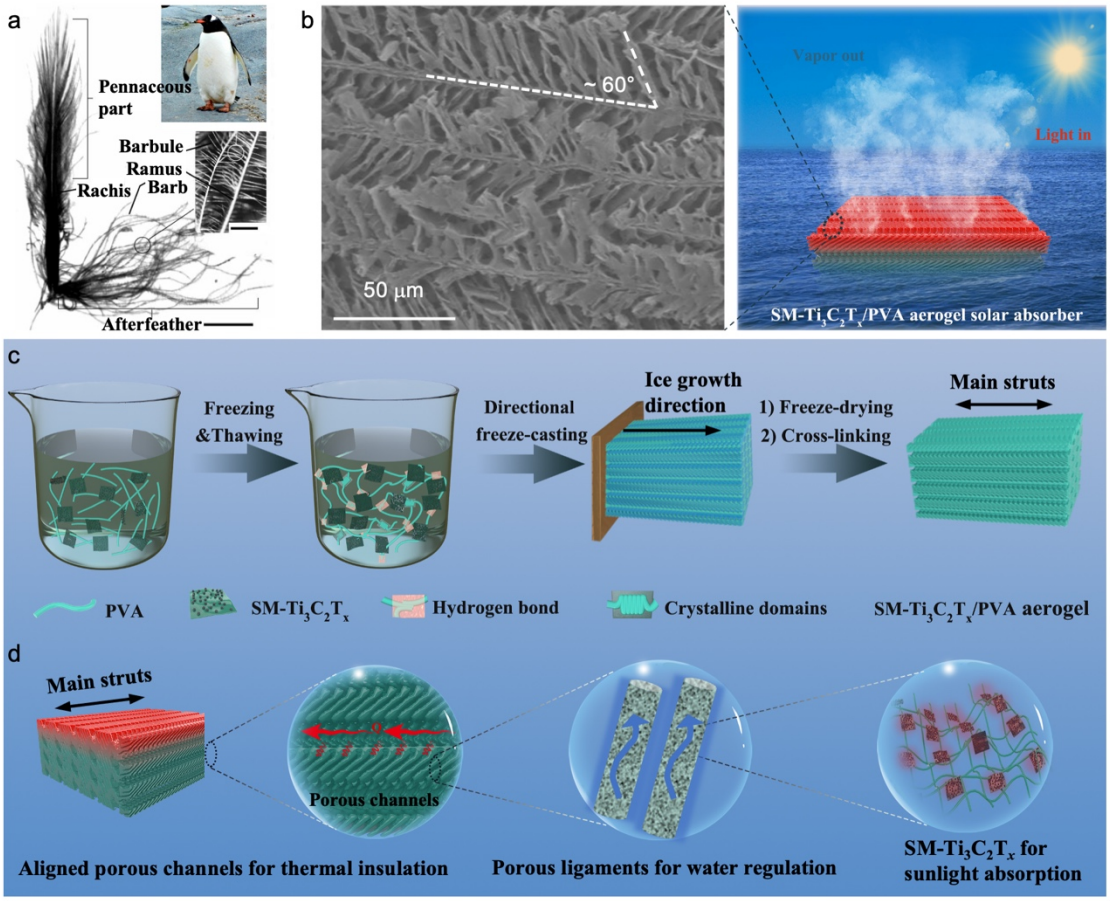

Figure 1. Biomimetic design and fabrication of the SM-$Ti_3C_2T_x$/PVA aerogel. (a) Photograph (Scale bar: 5 mm) and optical microscope image (inset, scale bar: 500 μm) of a penguin down-feather showing multiscale structural features. Reproduced with permission from ref. [49]. (b) Scanning electron microscope (SEM) image of the SM-$Ti_3C_2T_x$/PVA aerogel showing unique microstructure resembling that of the penguin down feather and schematic of its application for solar-powered water evaporation. Schematics showing (c) the fabrication and (d) multiscale, multifunctional structures of the SM-$Ti_3C_2T_x$/PVA aerogel.

2.2. Synthesis of SM-$Ti_3C_2T_x$ nanosheets

To improve the sunlight absorption of $Ti_3C_2T_x$ nanosheets, we introduced Ti^{3+}-TiO_2 and amorphous carbon nanoparticles on the surface of $Ti_3C_2T_x$ nanosheets by consecutive oxidation of $Ti_3C_2T_x$ and simple calcination processes, as shown in **Figure 2**a. The $Ti_3C_2T_x$ nanosheets were first exfoliated from Ti_3AlC_2 by selectively etching the Al layers using a mixture solution

of HCl and LiF.[55] The exfoliated $Ti_3C_2T_x$ nanosheets were dispersed in deionized (DI) water and stored at room temperature for 2 weeks to yield O-$Ti_3C_2T_x$ containing TiO_2 and amorphous carbon nanoparticles on their surface arising from the oxidation of $Ti_3C_2T_x$. The presence of TiO_2 was shown to have a negligible adverse effect on the photothermal conversion efficiency of $Ti_3C_2T_x$,[19] while the amorphous carbon had broadband light absorption because of its black appearance.[56] The O-$Ti_3C_2T_x$ nanosheets were heated to 350 °C in a N_2 atmosphere to reduce TiO_2 to Ti^{3+}-TiO_2 and obtain spectrally modified (SM)-$Ti_3C_2T_x$ nanosheets (see Experimental Section for details). The X-ray photoelectron spectroscopy (XPS) spectra indicate the presence of hydrophilic groups, such as -F and -OH functional groups, on the $Ti_3C_2T_x$ nanosheets after exfoliation (Figure S1). The SM-$Ti_3C_2T_x$ nanosheets were ultrathin and contained dispersed nanoparticles on their surface, as shown in **Figure 2**b-d. The high-resolution TEM (HRTEM) image (**Figure 2**c) revealed both crystalline Ti_3C_2 and amorphous carbon phases, substantiating the presence of carbon nanoparticles. The atomic force microscopy (AFM) image (**Figure 2**d) confirmed the surface decoration of nanoparticles on the SM-$Ti_3C_2T_x$ nanosheets with a typical thickness of 8.9 nm, corresponding to a few layers. The X-ray diffraction (XRD) spectra (**Figure 2**e) showed a downshift of the (002) peak from $2\theta = 9.5°$ to 6.42° after exfoliation, indicating expanded interlayer *d*-spacing of $Ti_3C_2T_x$ nanosheets from 9.3 to 13.0 Å. The *d*-spacing of SM-$Ti_3C_2T_x$ nanosheets further increased to 14.9 Å according to the reduce 2θ to 5.93° because of the possible intercalation of Ti^{3+}-TiO_2 and carbon particles into the interlayers. Additional diffraction peaks corresponding to the (101), (200), and (204) planes of anatase TiO_2 phase appeared in the SM-$Ti_3C_2T_x$ nanosheets owing to the existence of Ti^{3+}-TiO_2 nanoparticles.

To demonstrate the effectiveness of amorphous carbon and Ti^{3+}-TiO_2 nanoparticles, the optical absorptions of SM-$Ti_3C_2T_x$ and $Ti_3C_2T_x$ films were measured in the solar wavelengths ranging from 0.25 to 2.5 μm on an ultraviolet-visible near-infrared (UV-vis-NIR) spectrometer, as

shown in **Figure 2**f. According to the Air Mass (AM) 1.5 solar spectral irradiance (grey area), almost 90% of the total solar energy was emitted in the UV (from 0.25 to 0.4 μm), visible (from 0.4 to 0.7 μm) and IR-A (from 0.7 to 1.4 μm) wavelengths. This means that the broadband absorption in these wavelengths was imperative to impart a high energy efficiency. While the absorption of the $Ti_3C_2T_x$ film towards sunlight reached over 80% in the visible wavelengths in the range of 0.4 to 0.7 μm, those in the UV and IR-A wavelengths were much lower. After attaching amorphous carbon and Ti^{3+}-TiO_2 nanoparticles on the surface, the absorption of the SM-$Ti_3C_2T_x$ film was much improved in the whole wavelengths, reaching higher than 90% in the UV, visible, and IR-A ranges. The improved sunlight absorption of SM-$Ti_3C_2T_x$ was attributed to the synergy arising from the Ti^{3+}-TiO_2 and amorphous carbon nanoparticles. Ti^{3+}-TiO_2 absorbed significant UV light while amorphous carbon enhanced the absorption in the visible and NIR wavelengths. In sum, the successive oxidation and calcination of $Ti_3C_2T_x$ was a facile and effective strategy to enhance the absorption spectrum by introducing Ti^{3+}-TiO_2 and amorphous carbon nanoparticles on its surface.

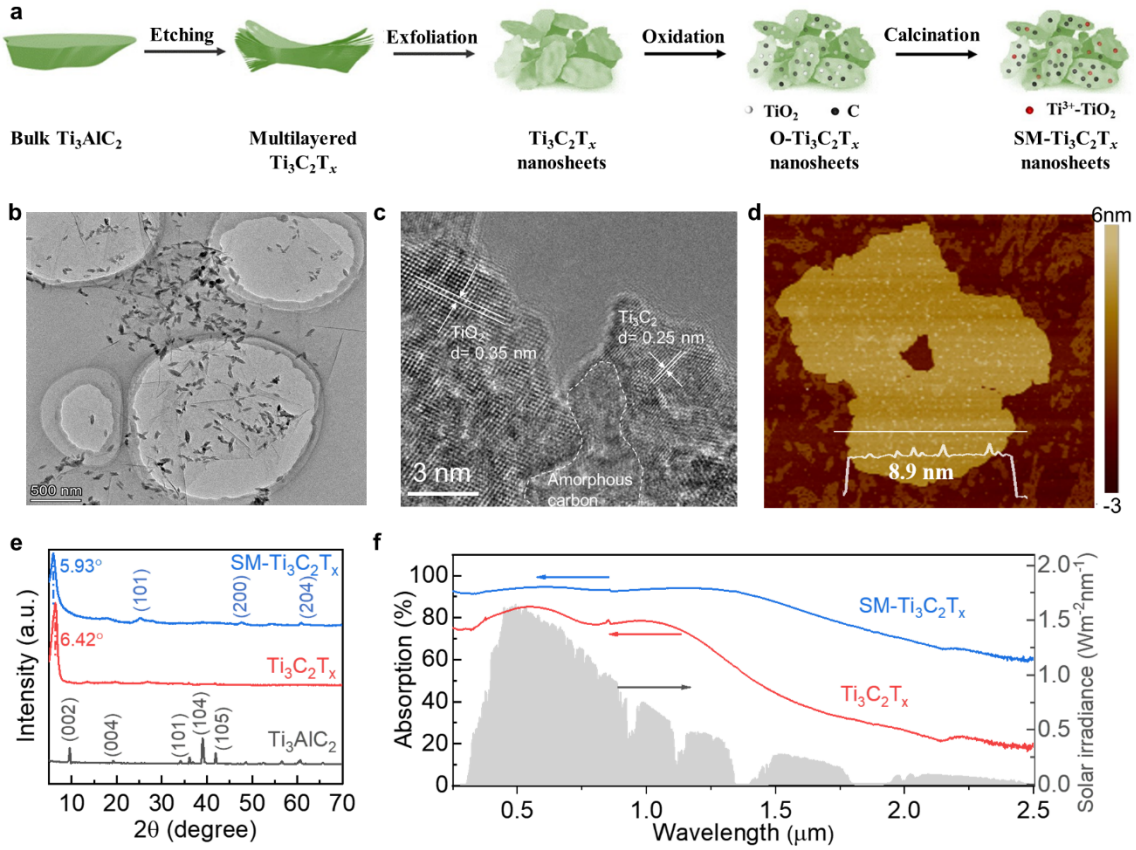

Figure 2. Synthesis and characterization of SM-$Ti_3C_2T_x$ nanosheets. (a) Schematic illustration of the synthesis of SM-$Ti_3C_2T_x$ nanosheets. (b) TEM, (c) HRTEM, and (d) AFM images of a SM-$Ti_3C_2T_x$ nanosheets. (e) XRD spectra of SM-$Ti_3C_2T_x$ nanosheets in comparison with $Ti_3C_2T_x$ and bulk Ti_3AlC_2. (f) Optical absorption spectra of SM-$Ti_3C_2T_x$ and $Ti_3C_2T_x$ films in the solar wavelengths. The grey area indicates the AM1.5 spectral irradiance according to the specification, ASTM G173-03.

2.3. Hierarchical porous structures of SM-$Ti_3C_2T_x$/PVA aerogels

The SM-$Ti_3C_2T_x$/PVA aerogels were fabricated by unidirectional freeze-casting of SM-$Ti_3C_2T_x$/PVA hydrogels followed by freeze-drying (**Figure 1**). The aerogel appeared black in color because of the SM-$Ti_3C_2T_x$ nanosheets (**Figure 3**a), indicating good absorption of visible light. The SEM image of the aerogel signifies an anisotropic hierarchical structure containing longitudinal main struts aligned in the freezing direction, *i.e.*, *y*-direction in **Figure 3**b, with parallel ligaments developed at an angle of ~ 60° from the main struts, yielding a unique 3D

feather-like network assembly. The presence of SM-$Ti_3C_2T_x$ nanosheets was confirmed by EDX elemental maps (**Figure 3**c), revealing the distribution of Ti, C, and O elements throughout the struts and ligaments. The unique feather-like microstructure was essential for simultaneous, multifunctional thermal and water managements to maximize the evaporation efficiency by virtue of its hierarchical porous structures, as shown in **Figure 3**d-f. The aerogel consisted of porous channels of ~ 50 μm in width, horizontally-aligned in the ice growth direction, i.e., *y*-direction, **Figure 3**d, which are sandwiched between main struts. Within the horizontal porous channels, abundant ligaments were formed at an angle of ~ 60° as a reflection of ice dendrite growth, further dividing the porous channels into microchannels of 10 to 20 μm in width in the transverse direction (**Figure 3**e). Inside the individual ligaments, smaller pores of less than 1 μm in size were also found (**Figure 3**f). Such a hierarchical porous structure was designed to offer simultaneously fast water transport, long-term self-floating, and excellent thermal insulation, as discussed in the following.

The unique hierarchical porous structure of the aerogel enabled excellent water regulation in both absorption and saturation. To achieve continuous supply of water for evaporation, the aerogel needs to efficiently absorb and transfer water to the evaporation surface while avoiding oversaturation to keep afloat on the water surface. The water absorption of the SM-$Ti_3C_2T_x$/PVA aerogel was measured by contact angle, as shown in **Figure 3**g. The water droplet was absorbed completely into the aerogel in only 6 s after dispensing thanks to the high porosity and hydrophilic surface of the $Ti_3C_2T_x$/PVA struts and ligaments. The absorbed water was subsequently transferred to the evaporation sites through the submicron pores in the transverse ligaments by capillary forces, warranting sufficient water uptake. Nevertheless, the water content could be oversaturated in the wet aerogel if too much water was absorbed, which in turn increased its density and thus potentially compromised the floatability.[57] Therefore, the water content in the wet aerogel has to be controlled to reduce its density well below that of

water, so as to keep it self-floating in the long term. To regulate the water content, the morphologies of SM-$Ti_3C_2T_x$/PVA aerogels were optimized by tuning the PVA/water ratio in the initial solution for freeze-casting, as shown in Figures S2 and 3h. With increasing PVA content from 0.06 to 0.18, the porosity tended to reduce consistently (Figure S2), leading to an upsurge in density of dry aerogel from 0.15 to 0.53 g cm^{-3} (**Figure 3**h). Meanwhile, the ability of aerogel to absorb water diminished because of the reduced porosity, resulting in a reduction in saturated water content in the aerogel with increasing PVA content. Consequently, the densities of wet aerogels measured after saturation with water for 24 h first decreased following the reduced saturated water content, and then increased along with the surge in density of dry aerogel. The aerogel made with a PVA/water ratio of 0.12 exhibited a density of 0.76 g cm^{-3}, far below that of water, even after full saturation with water.

To characterize the self-floating capabilities of wet aerogels, the dry aerogels were placed on the water surface to allow sufficient time to absorb water. The aerogel prepared with an optimal PVA/water ratio of 0.12 remained afloat after 24 h while the other two with the ratios lower or higher sank to the bottom of the container (Figure S3), consistent with the trend of their wet densities. In fact, the aerogel made from the optimal PVA content kept afloat for 15 days without sinking (Figure S4), ensuring long-term self-floating of the aerogel for practical applications without an extra supporting layer. The concurrent water transport and self-floating capabilities can be attributed to the unique hierarchical porous structure, as schematically shown in **Figure 3**i. The submicron pores in the hydrophilic ligaments allowed quick uptake of water through high capillary actions. The capillary force depends on the channel size, and a smaller channel size favors a larger capillary force for water uptake. Whereas the microchannels had large channel diameters of 10 – 20 μm (**Figure 3**e), the pores within the ligaments were much smaller with less than 1 μm in size (**Figure 3**f), generating a stronger capillary force than the microchannels. This means that the water tended to transport through

the pores inside the ligaments due to the stronger capillary force,[41] leaving behind air-filled microchannels for a low density and thus long-term self-floating even after water saturation (**Figure 3**i).

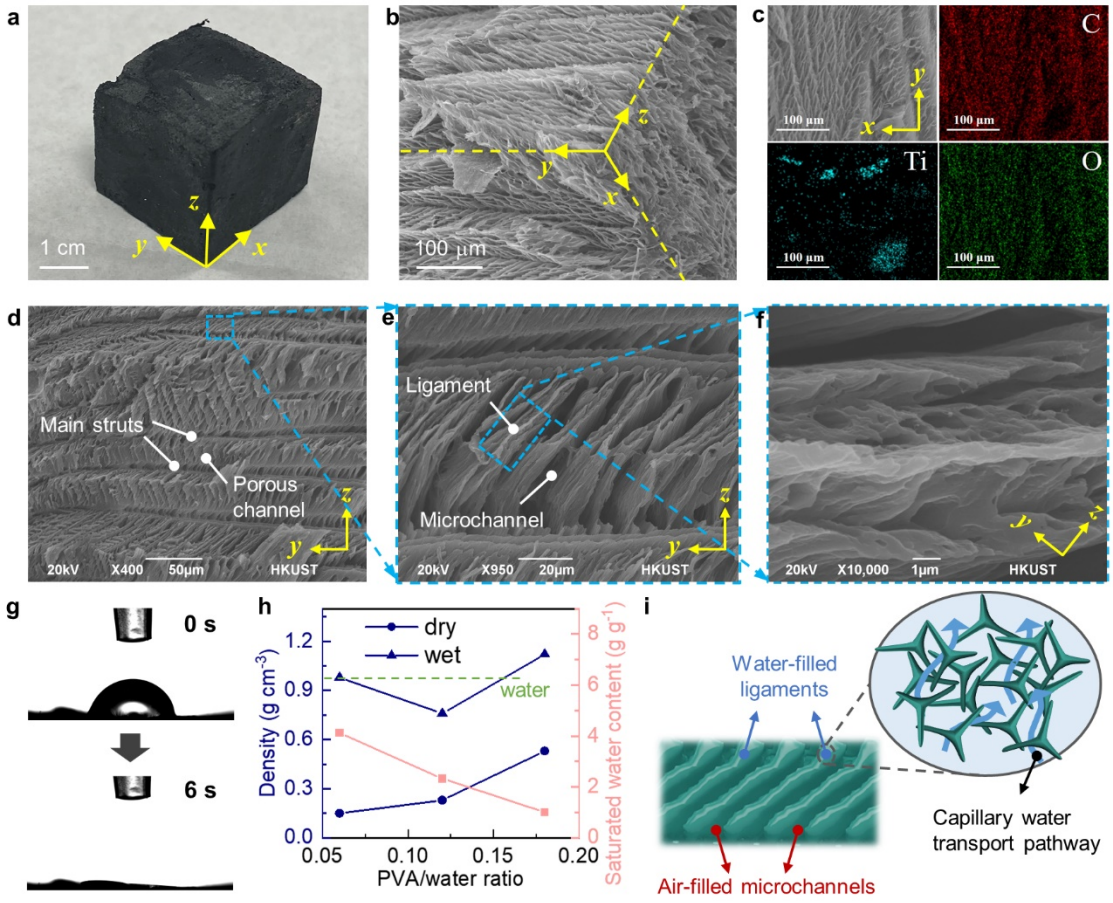

Figure 3. Structural characteristics and water regulation of the SM-$Ti_3C_2T_x$/PVA aerogel. (a) Optical, (b) SEM images, and (c) elemental EDX maps of the SM-$Ti_3C_2T_x$/PVA aerogel. The freeze-casting was carried out in the *y*-direction. SEM images of the SM-$Ti_3C_2T_x$/PVA aerogel taken from the y-z cross-section showing a hierarchical porous structure including (d) horizontally-aligned channels sandwiched between main struts, (e) transverse ligaments formed within the channel at an angle of 60° to main struts, and (f) and submicron pores within transverse ligaments. (g) Time-dependent contact angles of water with aerogel surface. (h) Densities of aerogels before absorbing water and after full saturation with water, and saturated

water contents in the aerogels as a function of PVA/water ratio. (i) Schematics of excellent water management of aerogel enabled by its hierarchical structure.

2.4. Thermal managements of SM-$Ti_3C_2T_x$/PVA aerogels

In addition to water managements, proper thermal managements are critical to a high energy efficiency of evaporation. To best utilize the solar energy for water evaporation, the absorption of sunlight in a full spectrum is required so as to maximize the heat gains from the sunlight while an ultralow thermal conductivity is essential to mitigate the heat losses (**Figure 4**a). The hierarchical porous structure endowed the SM-$Ti_3C_2T_x$/PVA aerogels with excellent thermal management capabilities in terms of sunlight absorption and thermal insulation.

The optical absorption and thermal conductivity of the SM-$Ti_3C_2T_x$/PVA aerogel with horizontally-aligned main struts (denoted as H-Gel, **Figure 4**b) were measured and compared with those containing vertically-aligned and randomly-distributed struts (denoted as V-Gel and R-Gel, respectively, **Figure 4**b) to highlight the advantages of the former structure. For the absorption measurements, all SM-$Ti_3C_2T_x$/PVA aerogel samples were in the wet state to reflect the practical evaporating condition. The neat PVA aerogel showed poor absorption towards sunlight while all composite aerogels containing SM-$Ti_3C_2T_x$ nanosheets exhibited absorptions of over 90% in the whole solar wavelengths from 0.25 to 2.5 μm (**Figure 4**c). The absorption of H-Gel was consistently higher than the V-Gel and R-Gel counterparts, achieving an exceptional full-spectrum absorption of 98.5 %. The stupendous performance of H-Gel arose not only from the inherent broadband absorption of SM-$Ti_3C_2T_x$ nanosheets (**Figure 2**f) but also from its hierarchical porous structure, which contributed to additional absorption by the multiple internal reflection of the penetrated sunlight through the parallel ligaments. Moreover, a water layer with a refractive index between air and SM-$Ti_3C_2T_x$ nanosheet was introduced in the wet H-Gel, reducing the reflection loss and thus leading to a higher absorption than the same H-Gel in a dry state (Figure S5).[58] The absorbed sunlight was efficiently converted to

heat thanks to the nearly 100% photothermal efficiency of $Ti_3C_2T_x$ nanosheets, raising the surface temperature of H-Gel to 64.3 °C under 1-sun irradiance, higher than those of V-Gel and R-Gel (Top-view, **Figure 4**d).

In addition to the full-spectrum sunlight absorption which facilitated the conversion of solar energy to heat, excellent thermal insulation was also necessary to concentrate the generated heat on the surface for a maximum solar-to-vapor efficiency. To assess the thermal insulation performance of different aerogels under service conditions, their thermal conductivities were measured in the thickness direction. Because they are easily wetted and exposed to high temperatures during evaporation, the measurements were made in both dry and wet states, as well as at different temperatures of 25 and 50 °C, as shown in **Figure 4**e. At 25 °C, the dry H-Gel showed a low thermal conductivity of 0.062 $Wm^{-1}K^{-1}$, 60% and 45% lower than those of V-Gel and R-Gel, respectively. When wetted by water, the thermal conductivity of H-Gel increased to 0.162 $Wm^{-1}K^{-1}$ reflecting the higher value ~ 0.6 $Wm^{-1}K^{-1}$ of water. Nonetheless, this value was still much lower than those of wet H-Gel (0.341 $Wm^{-1}K^{-1}$) and R-Gel (0.265 $Wm^{-1}K^{-1}$), consistent with the trend of their dry counterparts. The lower thermal conductivity of H-Gel can be attributed to the horizontally-aligned struts and the air-filled microchannels even when soaked with water, which significantly reduced the heat conduction in the thickness direction. On the contrary, the vertical struts in the V-Gel facilitated the heat transfer along the struts, giving rise to the highest thermal conductivity among the three. Notably, the thermal conductivities rose only slightly at 50 °C, suggesting that their thermal insulation properties could be well retained when high surface temperatures were expected under solar irradiation. The low thermal conductivity of H-Gel enabled a much steeper drop in temperature from the surface than the other gels (**Figure 4**f), effectively concentrating the generated heat on the evaporation surface (Side-view, **Figure 4**d).

In summary, the SM-$Ti_3C_2T_x$/PVA aerogel with horizontally aligned struts achieved both a full-spectrum sunlight absorption of 98.5 % and a low thermal conductivity of 0.162 $Wm^{-1}K^{-1}$ even when soaked with water thanks to the unique hierarchical porous structure. The combination of these properties is among the best when compared to other 3D solar absorbers reported in the literature, as shown in **Figure 4**g. Its extremely high sunlight absorption capability allowed effective solar-to-heat conversion while one of the lowest thermal conductivities mitigated the heat loss, synergistically contributing to a high energy efficiency for water evaporation. The all-inclusive water regulation and thermal managements achieved by the SM-$Ti_3C_2T_x$/PVA aerogel made it an ideal standalone evaporator without any support layers for floating, water transport, or thermal insulation, which in turn would significantly reduce the complexity for large-scale deployment in practical applications.

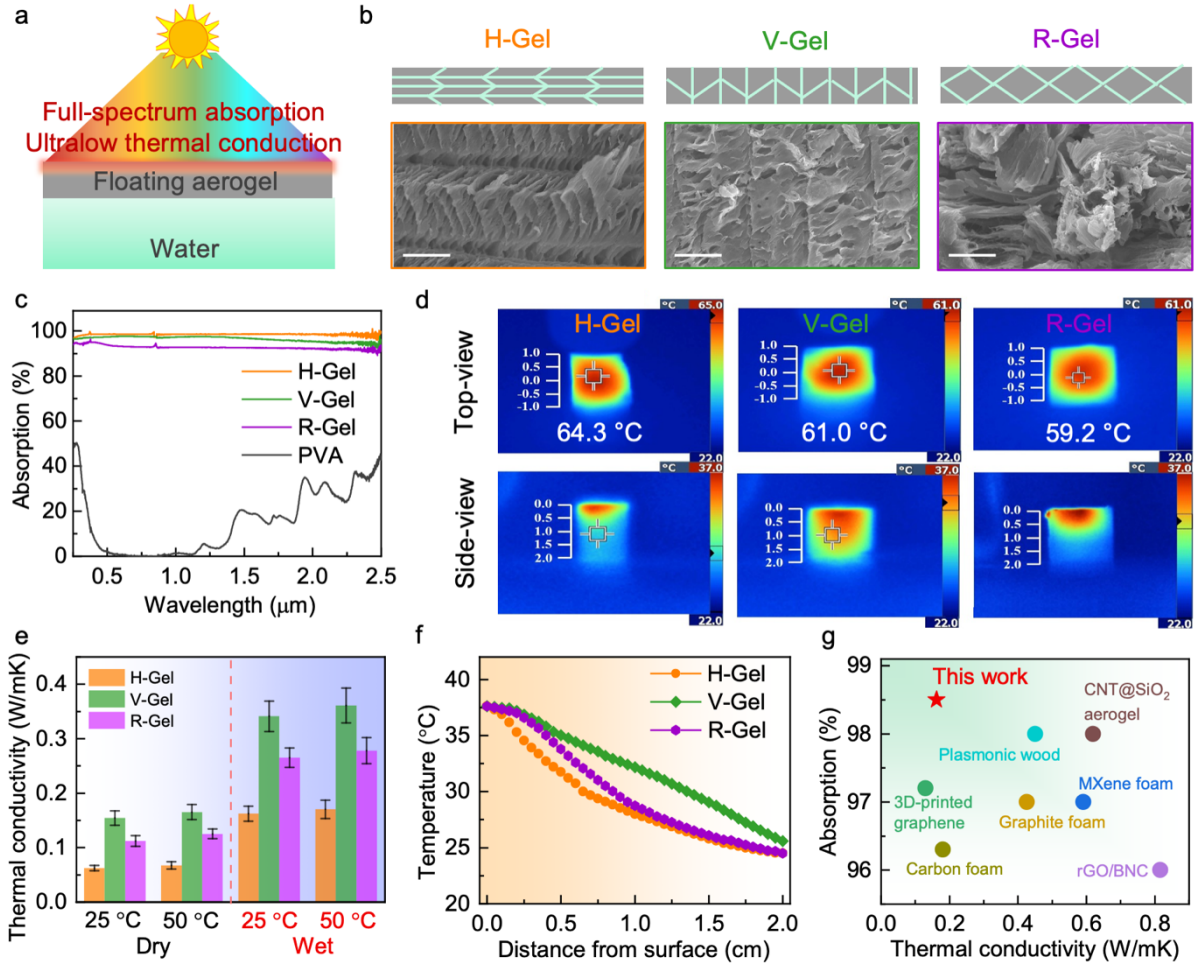

Figure 4. Thermal managements of SM-$Ti_3C_2T_x$/PVA aerogels. (a) Schematics of the thermal management strategies to maximize the solar-to-vapor energy efficiency. (b) Schematics and corresponding SEM images of the three aerogel structures with different morphologies. (c) Sunlight absorption, (d) infrared (IR) images under 1-sun irradiance, (e) thermal conductivities, and (f) temperature distributions along the thickness direction corresponding to the side-view IR images in (d) of three different aerogel structures. (g) Sunlight absorption and thermal conductivity of the SM-$Ti_3C_2T_x$/PVA aerogel in comparison with different 3D solar absorbers in the literature, including 3D-printed graphene,[14] carbon foam,[43] graphite foam,[59] rGO/bacteria nanocellulose (BNC) bilayer,[60] CNT@SiO_2 aerogel,[39] plasmonic wood,[3] and MXene foam.[18]

2.5. Solar-powered water evaporation performance of SM-$Ti_3C_2T_x$/PVA aerogels

The solar-powered water evaporation performance including the water evaporation rate and solar-to-vapor efficiency were measured using a custom-made setup (Figure S6). The SM-$Ti_3C_2T_x$/PVA aerogels were directly placed on the water surface to characterize its performance as a standalone evaporator. The change in surface temperature at a 1-sun irradiance was monitored with an IR camera, as shown in **Figure 5**a and b. The surface temperature of H-Gel initially rose quickly and then stabilized at around 42 °C after 360 s, the resulting temperature slightly higher than those of V-Gel and R-Gel, reflecting a better sunlight absorption capability of H-Gel. These surface temperatures were much higher than that of water surface, which remained at ~ 25 °C under the same solar intensity (grey line in **Figure 5**b). The higher surface temperature led to a faster water evaporation in H-Gel than its V- and R-Gel counterparts as well as neat water without any absorber, as evidenced by a more significant reduction of water mass with time during evaporation (**Figure 5**c). The corresponding evaporation rate of H-Gel was 1.83 kg m^{-2} h^{-1}, which was 7.9 times that of neat water and 12 and 16 % higher than those of R- and V-Gels, respectively (**Figure 5**d). Compared to the $Ti_3C_2T_x$/PVA aerogel, SM-

$Ti_3C_2T_x$/PVA aerogel showed a higher evaporation rate (Figure S7) because of the better sunlight absorption of SM-$Ti_3C_2T_x$ than $Ti_3C_2T_x$ (**Figure 2**f). To characterize the long-term stability and reusability of the SM-$Ti_3C_2T_x$/PVA aerogel, cyclic evaporation tests were carried out using the same H-Gel sample for 10 cycles, as shown in **Figure 5**e. The H-Gel was used as the absorber to evaporate sea water under 1-sun illumination for 3 hr in each cycle of tests. Then, the H-Gel was fully dried in an oven and reused for the next cycle of tests under the identical condition until a total of 10 cycles was completed. The high evaporation rate attained by H-Gel was maintained almost constant at 1.8 – 1.9 kg m^{-2} h^{-1} without apparent degradation for 10 cycles even when sea water was used, indicating an excellent reusability and stability of H-Gel for long-term, practical desalination applications.

The solar-to-vapor energy efficiency, η, was calculated by:

$$\eta = \frac{\dot{m}\Delta H_{equ}}{C_{opt}P_0} \quad (1)$$

where $\dot{m}$ is the mass flux of evaporated water, ΔH_{equ} is the equivalent vaporization enthalpy of water, C_{opt} is the optical concentration, and P_0 is the incident power density of 1-sun irradiance. The equivalent vaporization enthalpy of water in the presence of SM-$Ti_3C_2T_x$/PVA aerogel was measured by an evaporation test under the dark condition without sun radiation (Figure S8).[36] The enthalpy of water in the presence of aerogel was lower than that of water without aerogel because the intermediate water molecules adjacent to hydrophilic functional groups in PVA and $Ti_3C_2T_x$ nanosheets required less energy than water to evaporate.[36] It is noted that the mass flux was calculated based on the top projected area (i.e., the top surface area of 4 cm^2) and the dark evaporation rate was not subtracted because the side surfaces were not illuminated and the temperature of the aerogel was higher than the environment (Section S1 and Figure S9, Supporting Information).[61] The resulting solar-to-vapor energy efficiencies under 1-sun are shown in **Figure 5**d. The energy efficiency of H-Gel was 88.04 %, higher than both V-Gel and R-Gel following the trend of evaporation rates. Both the evaporation rate and energy efficiency

were directly correlated to the thermal management capabilities where H-Gel boasted the highest sunlight absorption and the lowest thermal conductivity among all materials tested (**Figure 4**c and e). This finding effectively substantiates the important role that the hierarchically porous structure of the SM-$Ti_3C_2T_x$/PVA aerogel with horizontally-aligned struts played.

The extraordinary thermal management performance of H-Gels was particularly pertinent to the energy efficiency under a weaker irradiance, where the same energy loss constituted a more significant portion of the total incident energy. The evaporation performance at a weaker irradiance can be practically more important because the intensity of natural sunlight is normally lower than 1-sun.[36,37] To demonstrate this, the energy efficiency and evaporation rate of H-Gel are compared with other standalone evaporators reported in the literature at two different solar irradiances, namely 1- and 0.5-sun, as shown in **Figure 5**f. The energy efficiency of H-Gel was comparable to those of state-of-the-art evaporators under 1-sun irradiance. However, the H-Gel delivered a high energy efficiency of 88.52 % under weak sunlight of 0.5-sun irradiance, much superior to previously reported evaporators which suffered generally low energy efficiencies below 85 %. The total theoretical heat loss due to radiation, convection and conduction was estimated to be 9.52 %, consistent with the high solar-to-vapor energy efficiency of 88.52 % obtained from the experiments (see detailed calculation in Section S2, Supporting Information). Combined with an evaporation rate of 0.92 kg m^{-2} h^{-1}, the overall evaporation performance of H-Gel at a more practical irradiance of 0.5-sun was the best among all the evaporators studied.

The exceptional energy efficiency of H-Gel under weak sunlight can be understood from its superior water and thermal management capabilities arising from the feather-like hierarchical porous structure, as illustrated in **Figure 5**g. The microchannels on the surface allowed multiple reflection of incident sunlight between ligaments containing SM-$Ti_3C_2T_x$ nanosheets for full-

spectrum sunlight absorption (**Figure 4**c), giving rise to a high solar-to-heat conversion efficiency. The converted heat was well confined on the surface because of the low thermal conductivity of wet H-Gel (**Figure 4**e) arising from the air-filled pores between ligaments thanks to the regulated water transport within the porous ligaments. Consequently, the heat losses originating from the sunlight reflection on the surface and heat conduction to the bulk water were minimized, leading to a high solar-to-vapor energy efficiency even at a weak irradiance of 0.5-sun. In particular, the H-Gel had several unique advantages over previous MXene- and PVA-based evaporators. First, the SM-$Ti_3C_2T_x$ nanosheets leveraged the natural oxidation process of $Ti_3C_2T_x$ to achieve a much-improved sunlight absorption, circumventing the addition of photothermal materials and the associated complex fabricating processes. Second, the feather-like hierarchical structure delivered an integrated solution to both thermal and water managements, avoiding additional insulating foams or dedicated water transport channels, thus making it ideal for large-scale deployment. Third, the PVA served not only as a hydrophilic component but also as an additive to regulate the ice growth in the ISFC technique, contributing to the unique feather-like microstructure completely different from the conventional unidirectional structure. The ISFC technique developed in this work can be widely applied to other material systems in controlling the alignments both along and transverse to the freezing direction.

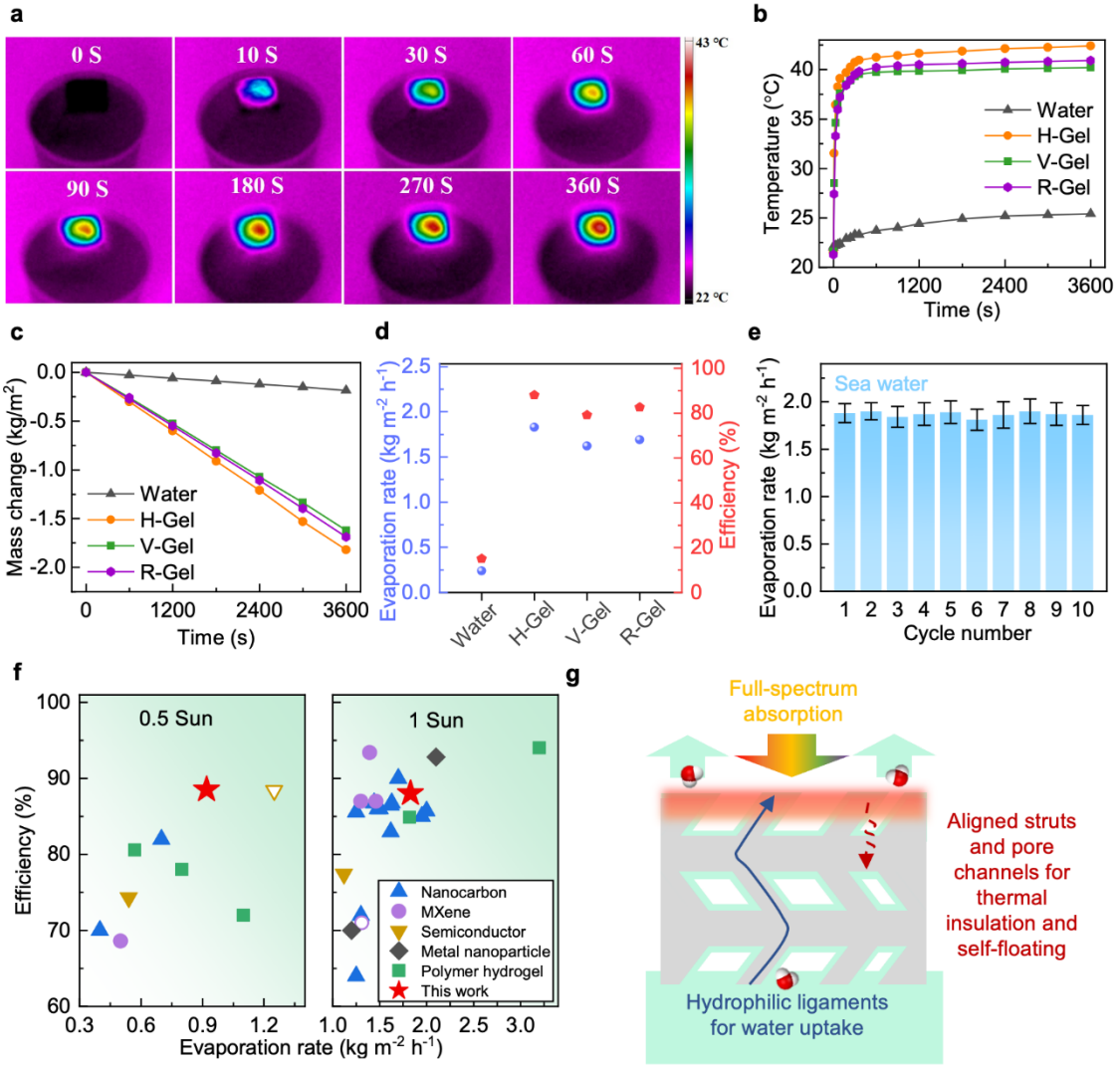

Figure 5. Evaporation performance of SM-$Ti_3C_2T_x$/PVA aerogels. (a) IR images showing the change in surface temperature of the SM-$Ti_3C_2T_x$/PVA aerogel under 1-sun irradiance. Changes in (b) surface temperature and (c) mass of three different aerogels as a function of time under 1-sun irradiance. (d) Evaporation rates and solar-to-vapor energy efficiencies of three different aerogels. (e) Evaporation rates of sea water attained by H-Gel for 10 cycles. (f) Comparison of energy efficiency and evaporation rate achieved using H-Gel under 0.5- and 1-sun with other evaporators made from different materials, including nanocarbon,[10,13,14,39,43,44,59,62–67] MXene,[18–21] semiconductors,[37,42] plasmonic nanoparticles,[3,4] and polymer hydrogels.[36,45,46,68] (g) Schematic of the mechanisms responsible for high energy efficiency and evaporation rate under weak irradiance.

The applications of the H-Gel evaporator for practical water desalination and purification under natural light and environment were further investigated. The resistance to salt accumulation is an important consideration for practical desalination as salts piled up on the evaporator surface are deleterious to both sunlight absorption and water transport.[69] The stable evaporation rates of the H-Gel evaporator tested in sea water (**Figure 5**e) indicate an excellent salt-rejecting capability, which was further confirmed by an outdoor experiment (Figure S10). The H-Gel was floated on top of a 3.5 wt% NaCl aqueous solution with 0.5 g solid NaCl powders initially placed on the evaporating surface to simulate the accumulated salts. During evaporation under natural sunlight, the NaCl powders were gradually re-dissolved in the water pumped up to the surface. The dissolved Na^+ and Cl^- ions then flowed back to the bulk NaCl solution through the highly porous water transport channels in the H-Gel, leaving almost no solid NaCl on the evaporating surface after 140 min. The salt-rejecting performance was mainly ascribed to the high porosity and hydrophilic SM-$Ti_3C_2T_x$/PVA struts and ligaments, facilitating the solvation and diffusion of salt ions back into the bulk water.[70] An evaporation-based desalination system was constructed using H-Gel evaporators to collect fresh water from seawater, as shown in **Figure 6**a and S11. The system was exposed to natural sunlight for 10 hr (from 8:00 to 18:00) on a typical sunny day in Hong Kong with the ambient air temperature and relative humidity recorded as a function of time, as shown in **Figure 6**b. The solar irradiance fluctuated during the day with an average value of 0.8 kW m^{-2}, generating an increasing amount of fresh water through evaporation (**Figure 6**c). The corresponding hourly evaporation rate followed the trend of solar irradiance, with an average energy efficiency of 86 % (**Figure 6**d). After 10 hr of evaporation during the daytime, the quantity of water obtained using the H-Gel evaporator with a surface area of 1 m^2 reached ~ 14 kg, enough for daily drinking water consumption of five individuals. The water also showed two to three orders of magnitude lower concentrations of ions after desalination, which are significantly lower than the maximum allowable thresholds

set by the World Health Organization (WHO) and the US Environmental Protection Agency (EPA) for drinking water (**Figure 6**e). In addition to desalination, the water purification capability was also assessed by incorporating Rhodamine B into the water to act as a pollutant. As shown in **Figure 6**f, the strong absorption peak corresponding to Rhodamine B at ~540 nm disappeared in the purified water, signifying the use of H-Gel evaporator offers an added benefit of water purification. The above results demonstrate the great potential of our SM-$Ti_3C_2T_x$/PVA aerogels for practical water desalination and purification.

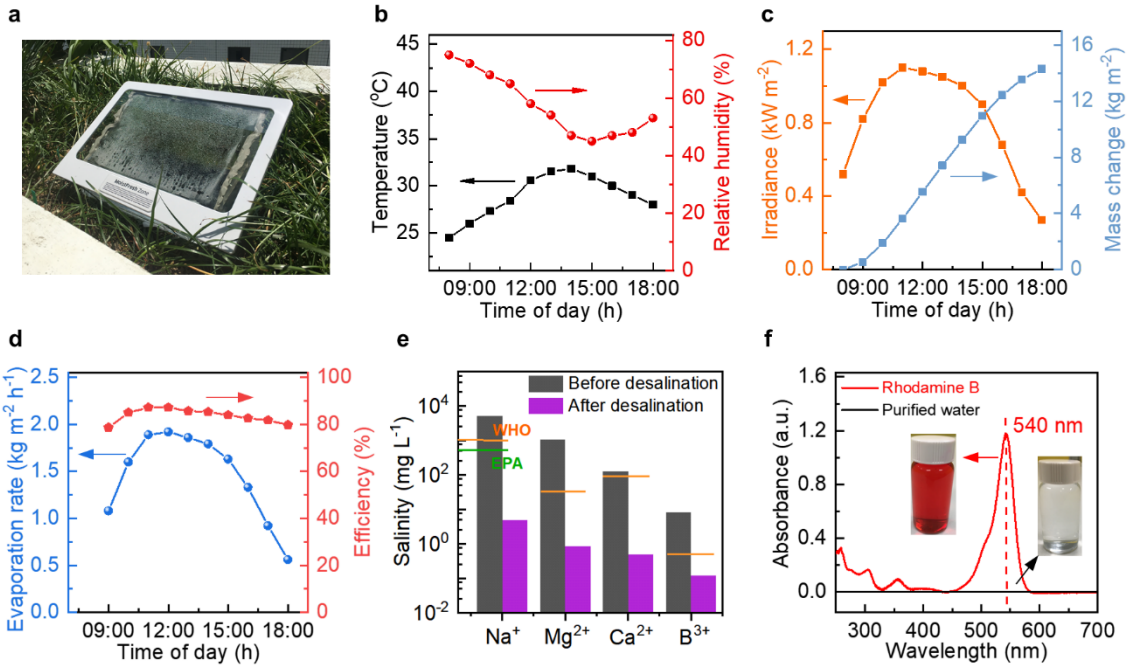

Figure 6. Demonstration of practical water desalination and purification under natural sunlight. (a) Photograph of the evaporation-based desalination system. (b) Air temperature and relative humidity, (c) solar irradiance and accumulated mass change of desalinated water, and (d) the corresponding evaporation rate and energy efficiency for evaporation from 8:00 to 18:00. (e) Concentrations of various ions measured in seawater before and after desalination. Orange and green lines represent the thresholds set by the WHO and the US EPA for drinking water. (f) Optical absorption spectra of DI water contaminated with Rhodamine B and purified water. The insets present optical images of contaminated water before and after purification.

3. Conclusion

In summary, a novel composite aerogel with a down feather-like hierarchical porous structure was designed and fabricated using SM-$Ti_3C_2T_x$ nanosheets for highly efficient solar-powered water evaporation. The SM-$Ti_3C_2T_x$ nanosheets were synthesized by successive oxidation and calcination of pristine $Ti_3C_2T_x$ nanosheets, which exhibited significantly augmented absorption spectra in the whole solar wavelengths compared to their pristine counterparts. The composite aerogel was rationally assembled from the SM-$Ti_3C_2T_x$ nanosheets based on the novel 'ice-structuring freeze-casting' technique using PVA as ice-structuring additive. The aerogel possesses a unique hierarchical porous structure containing horizontally aligned struts with parallel porous ligaments formed at an angle of ~ 60°, highly resembling the morphology of down feathers in penguins. Such a down feather-mimicking hierarchical structure gave rise to a low thermal conductivity of 0.062 $Wm^{-1}K^{-1}$ for the SM-$Ti_3C_2T_x$/PVA composite aerogel because of the horizontally-aligned pore channels with sizes of ~ 50 μm serving as effective thermal barriers. In addition, the transverse porous ligaments containing pores of ~1 μm in size effectively regulated the water transport in the vertical direction for efficient uptake of bulk water to the evaporation surface. Meanwhile, the dedicated water transport routes established through the ligaments were able to retain air-filled microchannels between them by discouraging excessive water to fill the channels for long-term self-floating and thermal insulation even when the aerogel was wet under service conditions. These microchannels also enhanced the absorption of incident sunlight through multiple reflection between their walls for more efficient sunlight absorption. Consequently, the low thermal conductivity of 0.162 $Wm^{-1}K^{-1}$ and full-spectrum sunlight absorption of 98.5 % constituted the best thermal management performance for the wet SM-$Ti_3C_2T_x$/PVA composite aerogel among standalone evaporators reported in the literature, leading to highly efficient solar thermal energy utilization especially under weak natural sunlight. An exceptional energy efficiency of 88.52 % with an

evaporation rate of 0.92 kg m^{-2} h^{-1} was achieved at a weak solar irradiance of 0.5-sun, demonstrating potential applications for practical solar-powered water desalination and purification under natural sunlight. The biomimetic hierarchical structure proposed in this work offers a new insight into integrated design of water regulation and thermal management using the same solar evaporator for reduced structural complexity and easy deployment.

4. Experimental Section

Materials: Titanium aluminum carbide (Ti_3AlC_2, 400 mesh) was supplied by Jilin 11 Technology, China. Chemicals including PVA (99+% hydrolyzed, molecular weight of 89,000 – 98,000), hydrochloric acid (37%), lithium fluoride (LiF) and sodium borohydride ($NaBH_4$, > 97.0 %) were supplied by Sigma-Aldrich. All the materials and chemicals were used without any treatment. The seawater was taken from the South China Sea near the HKUST.

Synthesis of SM-$Ti_3C_2T_x$ nanosheets: $Ti_3C_2T_x$ nanosheets were prepared by selectively etching the Al layers in Ti_3AlC_2 using a mixture of LiF and HCl. Typically, 2.0 g of Ti_3AlC_2 powders were slowly added to the mixture containing 2.0 g LiF and 40 mL HCl (9 M) in a 100 mL Teflon beaker, which was stirred gently at 35 °C for 24 h for etching of Al to take place. The resulting $Ti_3C_2T_x$ solution was washed and dispersed in DI water followed by mild ultrasonication. After centrifugation and washing, $Ti_3C_2T_x$ nanosheets were obtained which were stored at room temperature for 2 weeks for partial oxidation. Finally, the SM-$Ti_3C_2T_x$ nanosheets were synthesized by calcination. The oxidized $Ti_3C_2T_x$ nanosheets (0.2 g) and $NaBH_4$ (0.1 g) were mixed uniformly by grinding for 1 h. The mixture was then calcinated at 350 °C under a N_2 atmosphere for 1 h to obtain SM-$Ti_3C_2T_x$ nanosheets.

Fabrication of SM-$Ti_3C_2T_x$/PVA composite aerogels: The SM-$Ti_3C_2T_x$/PVA composite aerogels with a hierarchical porous structure were fabricated by directional freeze-casting followed by freeze-drying and subsequent thermo-crosslinking.[71,72] In a typical process, 12.0 g PVA powders were dissolved in 100 g DI water at 90 °C for 1 h. After cooling to room

temperature, SM-$Ti_3C_2T_x$ nanosheets were added into the PVA solution at a loading of 10 wt %. The mixture was mechanically stirred for 1 h followed by sonication for 10 min to uniformly disperse SM-$Ti_3C_2T_x$ nanosheets in the PVA solution. The SM-$Ti_3C_2T_x$ nanosheets/PVA solution was subjected to freezing-thawing cycles between -30 and 30 °C three times to form a crosslinked hydrogel. The SM-$Ti_3C_2T_x$/PVA hydrogel was poured into a plastic mold with a copper end immersed in liquid nitrogen for directional freeze-casting, followed by freeze-drying under vacuum for 48 hr to obtain SM-$Ti_3C_2T_x$/PVA aerogels with aligned main struts and transverse ligaments. Finally, the aerogels were transferred to an oven and heated at 90 °C for 1 hr. For comparison, SM-$Ti_3C_2T_x$/PVA aerogels with randomly distributed pores (denoted as R-Gel) were also prepared by placing a plastic mold containing the hydrogel in a freezer at -20 °C without directional freeze-casting.

Characterization: The morphologies of nanofillers and aerogels were characterized by SEM (JSM-6390, JEOL). HRTEM (Tecnai F30 G2, FEI) was used to study the morphologies of SM-$Ti_3C_2T_x$ nanosheets. AFM (MultiMode 8 system, Bruker) was used to characterize the thickness of nanosheets. XPS (SID-Elemental, Thermo Fisher Scientific) and FTIR (Vertex 70 Hyperion 1000, Bruker) were used to identify the chemical compositions and functional groups of SM-$Ti_3C_2T_x$ nanosheets. XRD (PANalytical, X'pert Pro) with a Cu-Kα (λ = 1.54059 Å) radiation source was used to confirm the crystallography of $Ti_3C_2T_x$ nanosheets. The sunlight absorption spectra of the aerogels were measured using a UV-Vis-NIR spectrophotometer (3700DUV, Shimadzu). The contact angles between the aerogels and water were evaluated using a goniometer (Attension Theta Lite, Biolin Scientific). The thermal conductivities of different aerogels were measured based on a transient plane heat source method (Hot Disk TPS2500S).

Solar-driven vapor generation experiments: Seawater was held in a glass vessel, and the SM-$Ti_3C_2T_x$/PVA composite aerogels were self-floated on the water surface. The temperature

change was monitored by a Fluke Ti25 Thermal Imager while the weight change of seawater was recorded every hr by an electronic mass balance (at an accuracy of 0.1 mg). The illumination was applied using a light source (MHAB-150W). The outdoor experiment was carried out using a large-scale homemade device with 0.05 m^2 in active area, as shown in Figure S11, with H-Gels under natural sunlight for 10 hr on 25 September 2019 in Hong Kong. 8 mm thick H-gels of 120 mm x 120 mm in square shape were placed on the surface of seawater. The solar intensity was measured by a solar power meter (ISM 410, ISO-TECH). The concentrations of ions were evaluated using an Inductively Coupled Plasma-Optical Emission Spectrometer (ICP-OES) (725-ES, Varian).

Acknowledgements

This project was financially supported by the Research Grants Council (GRF projects: 16209917, 16205517, and 16200720) and Innovation and Technology Commission (ITS/012/19) of Hong Kong SAR. Part of the work was performed when H.Z. was a visiting PhD student at HKUST from Northwestern Polytechnical University, China. Technical assistance from the Advanced Engineering Materials facilities (AEMF) and the Materials Characterization and Preparation Facilities (MCPF) is appreciated.

References

[1] M. Gao, L. Zhu, C. K. Peh, G. W. Ho, *Energy Environ. Sci.* **2019**, *12*, 841.

[2] F. Zhao, Y. Guo, X. Zhou, W. Shi, G. Yu, *Nat. Rev. Mater.* **2020**, *5*, 388.

[3] M. Zhu, Y. Li, F. Chen, X. Zhu, J. Dai, Y. Li, Z. Yang, X. Yan, J. Song, Y. Wang, E. Hitz, W. Luo, M. Lu, B. Yang, L. Hu, *Adv. Energy Mater.* **2018**, *8*, 1701028.

[4] Z. Sun, J. Wang, Q. Wu, Z. Wang, Z. Wang, J. Sun, C. Liu, *Adv. Funct. Mater.* **2019**, *29*, 1901312.

[5] J. Wang, Y. Li, L. Deng, N. Wei, Y. Weng, S. Dong, D. Qi, J. Qiu, X. Chen, T. Wu, *Adv. Mater.* **2017**, *29*, 1603730.

[6] M. Ye, J. Jia, Z. Wu, C. Qian, R. Chen, P. G. O'Brien, W. Sun, Y. Dong, G. A. Ozin, *Adv. Energy Mater.* **2017**, *7*, 1601811.

[7] X. Li, W. Xu, M. Tang, L. Zhou, B. Zhu, S. Zhu, J. Zhu, *Proc. Natl. Acad. Sci.* **2016**, *113*, 13953.

[8] J. Yang, Y. Pang, W. Huang, S. K. Shaw, J. Schiffbauer, M. A. Pillers, X. Mu, S. Luo, T. Zhang, Y. Huang, G. Li, S. Ptasinska, M. Lieberman, T. Luo, *ACS Nano* **2017**, *11*, 5510.

[9] Y. Ito, Y. Tanabe, J. Han, T. Fujita, K. Tanigaki, M. Chen, *Adv. Mater.* **2015**, *27*, 4302.

[10] H. Ren, M. Tang, B. Guan, K. Wang, J. Yang, F. Wang, M. Wang, J. Shan, Z. Chen, D. Wei, H. Peng, Z. Liu, *Adv. Mater.* **2017**, *29*, 1702590.

[11] Y. Yang, R. Zhao, T. Zhang, K. Zhao, P. Xiao, Y. Ma, P. M. Ajayan, G. Shi, Y. Chen, *ACS Nano* **2018**, *12*, 829.

[12] L. Cui, P. Zhang, Y. Xiao, Y. Liang, H. Liang, Z. Cheng, L. Qu, *Adv. Mater.* **2018**, *30*, 1706805.

[13] P. Zhang, J. Li, L. Lv, Y. Zhao, L. Qu, *ACS Nano* **2017**, *11*, 5087.

[14] Y. Li, T. Gao, Z. Yang, C. Chen, W. Luo, J. Song, E. Hitz, C. Jia, Y. Zhou, B. Liu, B. Yang, L. Hu, *Adv. Mater.* **2017**, *29*, 1700981.

[15] Y. Li, T. Gao, Z. Yang, C. Chen, Y. Kuang, J. Song, C. Jia, E. M. Hitz, B. Yang, L. Hu, *Nano Energy* **2017**, *41*, 201.

[16] D. Xu, Z. Li, L. Li, J. Wang, *Adv. Funct. Mater.* **2020**, *30*, 2000712.

[17] Z. Yu, P. Wu, *Adv. Mater. Technol.* **2020**, *5*, 2000065.

[18] X. Fan, Y. Yang, X. Shi, Y. Liu, H. Li, J. Liang, Y. Chen, *Adv. Funct. Mater.* **2020**,

30, 2007110.

[19] X. Zhao, L.-M. Peng, C.-Y. Tang, J.-H. Pu, X.-J. Zha, K. Ke, R.-Y. Bao, M.-B. Yang, W. Yang, *Mater. Horizons* **2020**, *7*, 855.

[20] J. Zhao, Y. Yang, C. Yang, Y. Tian, Y. Han, J. Liu, X. Yin, W. Que, *J. Mater. Chem. A* **2018**, *6*, 16196.

[21] Q. Zhang, G. Yi, Z. Fu, H. Yu, S. Chen, X. Quan, *ACS Nano* **2019**, *13*, 13196.

[22] W. Li, X. Li, W. Chang, J. Wu, P. Liu, J. Wang, X. Yao, Z.-Z. Yu, *Nano Res.* **2020**, *13*, 3048.

[23] K. Li, T. Chang, Z. Li, H. Yang, F. Fu, T. Li, J. S. Ho, P. Chen, *Adv. Energy Mater.* **2019**, *9*, 1901687.

[24] Y. Lu, D. Fan, Y. Wang, H. Xu, C. Lu, X. Yang, *ACS Nano* **2021**, *15*, 10366.

[25] X. Shen, J.-K. Kim, *Funct. Compos. Struct.* **2020**, *2*, 022001.

[26] X. Shen, Q. Zheng, J.-K. Kim, *Prog. Mater. Sci.* **2021**, *115*, 100708.

[27] Y. Wang, X. Wu, X. Yang, G. Owens, H. Xu, *Nano Energy* **2020**, *78*, 105269.

[28] X. Wu, Y. Wang, P. Wu, J. Zhao, Y. Lu, X. Yang, H. Xu, *Adv. Funct. Mater.* **2021**, *31*, 2102618.

[29] X. Wu, Z. Wu, Y. Wang, T. Gao, Q. Li, H. Xu, *Adv. Sci.* **2021**, *8*, 2002501.

[30] Y. Wang, X. Wu, B. Shao, X. Yang, G. Owens, H. Xu, *Sci. Bull.* **2020**, *65*, 1380.

[31] S. Wu, G. Xiong, H. Yang, B. Gong, Y. Tian, C. Xu, Y. Wang, T. Fisher, J. Yan, K. Cen, T. Luo, X. Tu, Z. Bo, K. (Ken) Ostrikov, *Adv. Energy Mater.* **2019**, *9*, 1901286.

[32] H. Liu, Z. Huang, K. Liu, X. Hu, J. Zhou, *Adv. Energy Mater.* **2019**, *9*, 1900310.

[33] M. Gao, C. K. Peh, L. Zhu, G. Yilmaz, G. W. Ho, *Adv. Energy Mater.* **2020**, *10*, 2000925.

[34] H. Wang, W. Xie, B. Yu, B. Qi, R. Liu, X. Zhuang, S. Liu, P. Liu, J. Duan, J. Zhou, *Adv. Energy Mater.* **2021**, *11*, 2100481.

[35] S. Chaule, J. Hwang, S. Ha, J. Kang, J. Yoon, J. Jang, *Adv. Mater.* **2021**, *33*, 2102649.

[36] F. Zhao, X. Zhou, Y. Shi, X. Qian, M. Alexander, X. Zhao, S. Mendez, R. Yang, L. Qu, G. Yu, *Nat. Nanotechnol.* **2018**, *13*, 489.

[37] Q. Lu, W. Shi, H. Yang, X. Wang, *Adv. Mater.* **2020**, *32*, 2001544.

[38] C. Lei, Z. Xie, K. Wu, Q. Fu, *Adv. Mater.* **2021**, 2103495.

[39] X. Dong, L. Cao, Y. Si, B. Ding, H. Deng, *Adv. Mater.* **2020**, *32*, 1908269.

[40] H. Liang, Q. Liao, N. Chen, Y. Liang, G. Lv, P. Zhang, B. Lu, L. Qu, *Angew. Chemie Int. Ed.* **2019**, *58*, 19041.

[41] Z. Wang, X. Wu, F. He, S. Peng, Y. Li, *Adv. Funct. Mater.* **2021**, *31*, 2011114.

[42] X. Feng, J. Zhao, D. Sun, L. Shanmugam, J.-K. Kim, J. Yang, *J. Mater. Chem. A* **2019**, *7*, 4400.

[43] C. Wang, J. Wang, Z. Li, K. Xu, T. Lei, W. Wang, *J. Mater. Chem. A* **2020**, *8*, 9528.

[44] Y. Lin, W. Zhou, Y. Di, X. Zhang, L. Yang, Z. Gan, *AIP Adv.* **2019**, *9*, 055110.

[45] Q. Chen, Z. Pei, Y. Xu, Z. Li, Y. Yang, Y. Wei, Y. Ji, *Chem. Sci.* **2018**, *9*, 623.

[46] J. Chen, B. Li, G. Hu, R. Aleisa, S. Lei, F. Yang, D. Liu, F. Lyu, M. Wang, X. Ge, F. Qian, Q. Zhang, Y. Yin, *Nano Lett.* **2020**, *20*, 6051.

[47] H. Liu, C. Chen, G. Chen, Y. Kuang, X. Zhao, J. Song, C. Jia, X. Xu, E. Hitz, H. Xie, S. Wang, F. Jiang, T. Li, Y. Li, A. Gong, R. Yang, S. Das, L. Hu, *Adv. Energy Mater.* **2018**, *8*, 1701616.

[48] P. Tao, W. Shang, C. Song, Q. Shen, F. Zhang, Z. Luo, N. Yi, D. Zhang, T. Deng, *Adv. Mater.* **2015**, *27*, 428.

[49] C. Dawson, J. F. . Vincent, G. Jeronimidis, G. Rice, P. Forshaw, *J. Theor. Biol.* **1999**, *199*, 291.

[50] S. Metwally, S. Martínez Comesaña, M. Zarzyka, P. K. Szewczyk, J. E. Karbowniczek, U. Stachewicz, *Acta Biomater.* **2019**, *91*, 270.

[51] N. Du, J. Fan, H. Wu, S. Chen, Y. Liu, *J. Theor. Biol.* **2007**, *248*, 727.

[52] Z. Wang, X. Shen, N. M. Han, X. Liu, Y. Wu, W. Ye, J.-K. Kim, *Chem. Mater.* **2016**, *28*, 6731.

[53] K. L. Scotti, D. C. Dunand, *Prog. Mater. Sci.* **2018**, *94*, 243.

[54] X. Liu, W. Xue, C. Shi, J. Sun, *Ceram. Int.* **2015**, *41*, 11922.

[55] E. Kim, H. Zhang, J.-H. Lee, H. Chen, H. Zhang, M. H. Javed, X. Shen, J.-K. Kim, *Compos. Part A Appl. Sci. Manuf.* **2021**, *147*, 106430.

[56] H. Yang, Z. Chen, Y. Xie, J. Wang, J. W. Elam, W. Li, S. B. Darling, *Adv. Mater. Interfaces* **2019**, *6*, 1801252.

[57] X. Zhou, Y. Guo, F. Zhao, W. Shi, G. Yu, *Adv. Mater.* **2020**, *32*, 2007012.

[58] Y. Wang, X. Wu, T. Gao, Y. Lu, X. Yang, G. Y. Chen, G. Owens, H. Xu, *Nano Energy* **2021**, *79*, 105477.

[59] H. Ghasemi, G. Ni, A. M. Marconnet, J. Loomis, S. Yerci, N. Miljkovic, G. Chen, *Nat. Commun.* **2014**, *5*, 4449.

[60] Q. Jiang, L. Tian, K.-K. Liu, S. Tadepalli, R. Raliya, P. Biswas, R. R. Naik, S. Singamaneni, *Adv. Mater.* **2016**, *28*, 9400.

[61] X. Li, G. Ni, T. Cooper, N. Xu, J. Li, L. Zhou, X. Hu, B. Zhu, P. Yao, J. Zhu, *Joule* **2019**, *3*, 1798.

[62] W. Xu, Y. Xing, J. Liu, H. Wu, Y. Cui, D. Li, D. Guo, C. Li, A. Liu, H. Bai, *ACS Nano* **2019**, *13*, 7930.

[63] P. Mu, Z. Zhang, W. Bai, J. He, H. Sun, Z. Zhu, W. Liang, A. Li, *Adv. Energy Mater.* **2019**, *9*, 1802158.

[64] W. Xu, X. Hu, S. Zhuang, Y. Wang, X. Li, L. Zhou, S. Zhu, J. Zhu, *Adv. Energy Mater.* **2018**, *8*, 1702884.

[65] C.-S. Hu, H.-J. Li, J.-Y. Wang, A. Haleem, X.-C. Li, M. Siddiq, W.-D. He, *ACS Appl.*

Energy Mater. **2019**, *2*, 7554.

[66] X. Song, H. Song, S. Wang, J. Liu, L. Zhou, J. Xu, K. Chen, *J. Mater. Chem. A* **2019**, *7*, 26496.

[67] X. Hu, W. Xu, L. Zhou, Y. Tan, Y. Wang, S. Zhu, J. Zhu, *Adv. Mater.* **2017**, *29*, 1604031.

[68] N. Li, L. Qiao, J. He, S. Wang, L. Yu, P. Murto, X. Li, X. Xu, *Adv. Funct. Mater.* **2020**, 2008681.

[69] G. Liu, T. Chen, J. Xu, G. Yao, J. Xie, Y. Cheng, Z. Miao, K. Wang, *Cell Reports Phys. Sci.* **2021**, *2*, 100310.

[70] Y. Kuang, C. Chen, S. He, E. M. Hitz, Y. Wang, W. Gan, R. Mi, L. Hu, *Adv. Mater.* **2019**, *31*, 1900498.

[71] F. Guo, X. Shen, J. Zhou, D. Liu, Q. Zheng, J. Yang, B. Jia, A. K. T. Lau, J. Kim, *Adv. Funct. Mater.* **2020**, *30*, 1910826.

[72] Y. Wu, Z. Wang, X. Shen, X. Liu, N. M. Han, Q. Zheng, Y.-W. Mai, J.-K. Kim, *ACS Appl. Mater. Interfaces* **2018**, *10*, 26641.

Table of Content

A novel, penguin feather-like MXene aerogel absorber with multifunctional capabilities of excellent thermal insulation and water uptake is developed. It delivers a high energy efficiency of 88.52 % and an evaporation rate of 0.92 kg m^{-2} h^{-1} at 0.5-sun irradiance, promising its great potential for practical solar-powered water desalination and purification under natural sunlight.

Hongming Zhang, Xi Shen, Eunyoung Kim, Mingyue Wang, Jeng-Hun Lee, Haomin Chen, Guangcheng Zhang, Jang-Kyo Kim**

Integrated water and thermal managements in bioinspired hierarchical MXene aerogels for highly efficient solar-powered water evaporation